Water Resources Research

RESEARCH ARTICLE
10.1029/2023WR034535

Fast and Accurate Estimation of Evapotranspiration for Smart Agriculture

Weiyu Li[1] **and Daniel M. Tartakovsky**[1]

[1]Department of Energy Science and Engineering, Stanford University, Stanford, CA, USA

Key Points:

- Current strategies for evapotranspiration estimations from moisture sensors rely on the vertical-flow assumption, which fails for drip irrigation
- Our implementations of ensemble Kalman filter (EnKF) and maximum likelihood estimation overcome this limitation
- Both methods outperform the standard EnKF approach, which updates soil moisture, by up to two orders of magnitude

Correspondence to:
D. M. Tartakovsky,
tartakovsky@stanford.edu

Citation:
Li, W., & Tartakovsky, D. M. (2023). Fast and accurate estimation of evapotranspiration for smart agriculture. *Water Resources Research*, *59*, e2023WR034535. https://doi.org/10.1029/2023WR034535

Received 20 JAN 2023
Accepted 4 APR 2023

Author Contributions:
Conceptualization: Weiyu Li, Daniel M. Tartakovsky
Data curation: Weiyu Li
Formal analysis: Weiyu Li
Funding acquisition: Daniel M. Tartakovsky
Investigation: Weiyu Li
Methodology: Weiyu Li
Project Administration: Daniel M. Tartakovsky
Resources: Daniel M. Tartakovsky
Software: Weiyu Li
Supervision: Daniel M. Tartakovsky
Visualization: Weiyu Li
Writing – original draft: Weiyu Li
Writing – review & editing: Daniel M. Tartakovsky

Abstract The ability to quantify evapotranspiration (ET) is crucial for smart agriculture and sustainable groundwater management. Efficient ET estimation strategies often rely on the vertical-flow assumption to assimilate data from soil-moisture sensors. While adequate in some large-scale applications, this assumption fails when the horizontal component of the local flow velocity is not negligible due to, for example, soil heterogeneity or drip irrigation. We present novel implementations of the ensemble Kalman filter (EnKF) and the maximum likelihood estimation (MLE), which enable us to infer spatially varying ET rates and root water uptake profiles from soil-moisture measurements. While the standard versions of EnKF and MLE update the predicted soil moisture prior to computing ET, ours treat the ET sink term in Richards' equation as an updatable observable. We test the prediction accuracy and computational efficiency of our methods in a setting representative of drip irrigation. Our strategies accurately estimate the total ET rates and root-uptake profiles and do so up to two-orders of magnitude faster than the standard EnKF.

Plain Language Summary The ability to quantify evapotranspiration (ET) is crucial for smart agriculture and sustainable groundwater management. We present novel implementations of the ensemble Kalman filter and the maximum likelihood estimation, which enable us to infer spatially varying ET rates and root water uptake profiles from soil-moisture measurements. We test the prediction accuracy and computational efficiency of our methods in a setting representative of drip irrigation. Our strategies accurately estimate the total ET rates and root-uptake profiles and do so up to two-orders of magnitude faster than the standard techniques.

1. Introduction

Smart agriculture relies on modern data collection and analysis technologies to reduce water consumption and increase crop yield. In the process, the data collected by a network of soil-moisture sensors are used to improve predictions of infiltration rate (Wang & Tartakovsky, 2011), wetting depth (Sinsbeck & Tartakovsky, 2015), evapotranspiration (ET) rate (Li et al., 2021), etc. We focus on ET estimation, because its improved accuracy is pivotal to the optimization of crop irrigation (Martín et al., 2021), the assessment of the impact of inundation (Ban et al., 2018), etc. A prime example of such strategies for sustainable development is drip irrigation, which is mainly deployed in areas facing severe water scarcity (Lamm et al., 2012; Latif et al., 2016), for crops such as cotton and maize (Sampathkumar et al., 2012). Around 2.9 million acres of croplands in California are equipped with drip irrigation systems, which make up about 60% of all drip irrigation in the US (Anderson, 2019).

Data-driven estimation of ET usually invokes the assumption of vertical, one-dimensional (1D) flow, such that soil-moisture sensors are placed within a 1D soil column with homogeneous soil properties (Breña Naranjo et al., 2011; Galleguillos et al., 2017; Parajuli et al., 2019). A key advantage of ensemble-based (Bayesian) data assimilation (DA) methodologies is that their estimates of the relevant system parameters and state variables are equipped with uncertainty (error) bounds (Boso & Tartakovsky, 2022). Among these tools, ensemble Kalman filter (EnKF) has gained popularity because of computational expediency; among other hydrologic applications, it was used to estimate, from soil-moisture sensor-array data, water content and *total* ET rate (Pan & Wood, 2006; Reichle et al., 2008) and *spatial distributions* of ET rates and root water-uptake (Li et al., 2021) in vertical (1D) soil columns.

The vertical-flow assumption alleviates the computational cost of ensemble-based DA techniques, for example, variational DA, EnKF and particle filters, and is arguably adequate at the basin scale. At the field scale of interest to smart agriculture, the 1D assumption implies a homogeneous soil with sprinkler/spray irrigation patterns that are similar to rainfall. It stands to reason that this assumption fails for drip irrigation, which results in two- or

three-dimensional (2D or 3D) infiltration patterns. Local soil heterogeneity magnifies the horizontal component of the flow velocity regardless of the irrigation pattern. To alleviate the high computational cost of 2D or 3D ensemble-based computations, the relatively few attempts to estimate total ET rates from soil-moisture data found it necessary to replace the numerical solution of the 2D/3D Richards equation with the water balance approach (Karandish & Šimůnek, 2016; He et al., 2018; do Nascimento et al., 2021). This strategy is not designed to capture the spatiotemporal root water uptake profile, except during the dry period (Hupet et al., 2002).

Our goal is to design computationally efficient implementations of EnKF and maximum likelihood estimation (MLE) to infer the ET rate from soil-moisture data in high-dimensional settings relevant to smart agriculture. We extend the DA methodologies of Li et al. (2021) from 1D to higher dimensions. By treating the sink (ET) term in the Richards equation as a state variable, which is being updated during the DA procedure, these 1D techniques achieve the up to two orders of magnitude computational speedup vis-à-vis their standard counterparts that update soil moisture. We use a series of numerical experiments to demonstrate that similar speed-up is observed in a 2D heterogeneous soil (10 m in width and 1.5 m in depth) with a spatially varying root density function, a setting representative of drip irrigation (do Nascimento et al., 2021).

Starting with a problem description (Section 2), we formulate our DA methodologies in a fully vectorized form suitable for high dimensions (Section 3). In Section 4, we generate a synthetic 2D agricultural plot, for which the soil moisture is computed by solving numerically the Richards equation with a known sink term; a sensor network is deployed to collect the soil moisture data (the known solution corrupted by measurement noise) for a period of time during which several cycles of drip irrigation take place. Our versions of EnKF and MLE are used in Section 5 to reconstruct the sink term from these sparse and noisy data; the comparison with the sink terms used to generate the data allows us to ascertain the prediction accuracy and computational efficiency of both methods. Main conclusions of this study are summarized in Section 6.

2. Problem Formulation

We assume that volumetric water content $\theta(\mathbf{x}, t)$ and pressure head $\psi(\mathbf{x}, t)$, at any time $t > 0$ and point $\mathbf{x} = (x, z)^\top \in \Omega$ within an agricultural plot Ω, can be predicted with the 2D Richards equation,

$$\frac{\partial \theta}{\partial t} = \nabla \cdot [\mathbf{K}(\mathbf{x}, \psi)\nabla(\psi - z)] - T(\mathbf{x}, t, \theta), \qquad \mathbf{x} \in \Omega, \quad t > 0. \tag{1}$$

Here, x is the horizontal coordinate; z is the vertical coordinate indicating the distance from the soil surface ($z = 0$) and being positive downward; and the soil domain Ω has depth L_z and width L_x, such that $\Omega = \{\mathbf{x}: 0 < x < L_x, 0 < z < L_z\}$. To account for the soil's anisotropy and heterogeneity, we treat its unsaturated hydraulic conductivity $\mathbf{K}(\mathbf{x}, \psi)$ as the second-rank tensor,

$$\mathbf{K}(\mathbf{x}, \psi) = \mathbf{K}_s(\mathbf{x})K_r(\psi) = \begin{bmatrix} K_x(\mathbf{x}) & 0 \\ 0 & K_z(\mathbf{x}) \end{bmatrix} K_r(\psi), \tag{2}$$

where $\mathbf{K}_s$ is the saturated hydraulic conductivity tensor with the horizontal and vertical components K_x and K_z, respectively; and $K_r(\psi)$ is the relative hydraulic conductivity. The sink term, $T(\mathbf{x}, t, \theta)$, in Equation 1 represents plant transpiration, aka root water uptake function.

The Richards equation is closed by specifying the three constitutive relations $\theta = \theta(\psi)$, $K_r = K_r(\psi)$, and $T = T(\theta)$. To be specific, we select the van Genuchten model (van Genuchten, 1980) for the first two,

$$K_r = \frac{\left[1 - \psi_d^{mn}\left(1 + \psi_d^n\right)^{-m}\right]^2}{\left(1 + \psi_d^n\right)^{m/2}}, \qquad \frac{\theta - \theta_i}{\phi - \theta_i} = \left(1 + \psi_d^n\right)^{-m}, \tag{3}$$

where $\psi_d = \alpha_{vG}|\psi|$, $n = 1/(1 - m)$, θ_i is the irreducible water content; ϕ is the porosity; α_{vG} and m are the shape (fitting) parameters. For the third relation, we use a canonical form (Perrochet, 1987; Vrugt, van Wijk, et al., 2001),

$$T(\mathbf{x}, t, \theta) = F_{root}(\mathbf{x})L_x T_{max}(t)\gamma_T(\theta), \tag{4a}$$

where $T_{max}(t)$ is the potential transpiration rate with units of length over time;

$$\gamma_T(\theta) = \begin{cases} 0 & 0 \le \theta < \theta_w \\ \dfrac{\theta - \theta_w}{\theta^* - \theta_w} & \theta_w < \theta \le \theta^* \\ 1 & \theta^* < \theta \le \theta_p \end{cases} \tag{4b}$$

is the root uptake water-stress response function (Guswa et al., 2002; Porporato et al., 2003) parameterized by the water content at the wilting point, θ_w, the water content at the point of stomatal closure, θ^*, at which the uptake equals the demand, and by the field capacity θ_p; and

$$F_{root}(\mathbf{x}) = \frac{\mathcal{F}_{root}(\mathbf{x})}{\int_\Omega \mathcal{F}_{root}(\mathbf{x})d\mathbf{x}} \tag{4c}$$

is the normalized 2D root density function with units of one over length squared. For a single plant located at $\mathbf{x}_p = (x_p, 0)^\top$ and having the maximum rooting length x_m and depth z_m, the 2D root density function $\mathcal{F}_{root}(\mathbf{x}; \mathbf{x}_p)$ is given by (Vrugt, Hopmans, et al., 2001)

$$\mathcal{F}_{root}(\mathbf{x}; \mathbf{x}_p) = \left[1 - \frac{\min(|x - x_p|, x_m)}{x_m}\right]\left[1 - \frac{\min(z, z_m)}{z_m}\right] e^{-p_x|x^* - |x - x_p||/x_m - p_z|z^* - z|/z_m}, \tag{4d}$$

where $\mathbf{x}^* = (x^*, z^*)^\top$ is the location of the maximum root water uptake, and p_x and p_z are the shape factors (fitting parameters). For N_p plants placed at locations $\mathbf{x}_{p_i} = (x_{p_i}, 0)^\top$ with $i = 1, \ldots, N_p$, we generalize the above expression to read

$$\mathcal{F}_{root}(\mathbf{x}) = \sum_{i=1}^{N_p} \mathcal{F}_{root}(\mathbf{x}; \mathbf{x}_{p_i}). \tag{4e}$$

While evaporation can occur over a finite soil depth, we follow the standard practice by restricting it to the soil surface. For an array of N_d drip emitters located at $\mathbf{x}_{d_k} = (x_{d_k}, 0)^\top$ with $k = 1, \ldots, N_d$, this approximation gives rise to the boundary condition at $z = 0$,

$$K_z K_r(\theta)\left(\frac{\partial \psi}{\partial z} - 1\right) = P(t) L_d \sum_{k=1}^{N_d} \delta(x - x_{d_k}) - E(\theta, t), \qquad 0 \le x \le L_x, \quad t > 0, \tag{5}$$

where $P(t)$ is the flow rate of the drip emitter, with units of length per time; L_d is the characteristic length of the dripping device; $\delta(\cdot)$ is the Dirac delta function; and the evaporation rate $E(\theta, t)$ is modeled, in analogy to Equation 4, as

$$E(\theta(\mathbf{x}, t), t) = E_{max}(t)\gamma_E(\theta(\mathbf{x}, t)), \qquad \text{for } \mathbf{x} = (x, 0)^\top. \tag{6a}$$

Here, E_{max} is the maximum evaporation rate, and the evaporation reduction factor γ_E is given by (Hale & Orcutt, 1987)

$$\gamma_E(\theta(x, 0, t)) = \begin{cases} 0 & 0 \le \theta(x, 0, t) < \theta_h \\ \dfrac{\theta(x, 0, t) - \theta_h}{\theta_w - \theta_h} & \theta_h < \theta(x, 0, t) \le \theta_w \\ 1 & \theta_w < \theta(x, 0, t) \le \theta_p, \end{cases} \tag{6b}$$

where θ_h is the hygroscopic saturation at which evaporation diminishes. At the bottom of the soil domain, $z = L_z$, we impose a free-drainage condition,

$$\frac{\partial \psi}{\partial z} - 1 = 0, \qquad 0 \le x \le L_x, \quad z = L_z, \quad t > 0, \tag{7}$$

The boundary conditions on the remaining segments of the computational domain are

$$\frac{\partial \psi}{\partial x} = 0, \qquad \text{for } x = 0 \text{ and } L_x, \quad 0 < z < L_z, \quad t > 0. \tag{8}$$

Finally, we assume the initial water content in the soil domain, θ_0, to be uniform, giving rise to the initial condition

$$\theta(\mathbf{x} \in \Omega, 0) = \theta_0. \tag{9}$$

In the flow model given by Equations 1–9, we assume the static soil properties (e.g., the saturated hydraulic conductivity $\mathbf{K}_s(\mathbf{x})$ and the van Genuchten parameters α_{vG} and n) and the root density distribution $\mathcal{F}_{root}(\mathbf{x})$ to be known with certainty (e.g., estimated in advance through infiltration tests). Our goal is to estimate the maximum evaporation rate $E_{max}(t)$ and the potential transpiration rate $T_{max}(t)$ from soil-moisture data collected by a sensor network. These two functions in Equations 4a and 6a parameterize the ET rate (1/hr),

$$S(\mathbf{x}, t) = T(\mathbf{x}, t, \theta(\mathbf{x}, t)) + E(\mathbf{x}, t, \theta(\mathbf{x}, t))\delta(z), \qquad z \geq 0. \tag{10}$$

In numerical simulations, the soil domain Ω is discretized with a rectangular mesh consisting of N_{row} rows and N_{col} columns, for the total of $N_{el} = N_{row} \times N_{col}$ elements. The sides of each element are Δx and Δz in the x and z directions, respectively; discrete times $\tau_i = i\Delta t$ ($i = 0, 1, 2, \ldots$) are separated by the time step Δt. We arrange the numerical solution of Equations 1–9, $\theta(\mathbf{x}_l, \tau_i)$ with $l = 1, \ldots, N_{el}$ and $i = 0, 1, 2, \ldots$, in the form of a vector of length N_{el}:

$$\boldsymbol{\theta}(\tau_i) = \left(\theta_{(1,1)}, \ldots, \theta_{(N_{row},1)}, \ldots, \theta_{(1,N_{col})}, \ldots, \theta_{(N_{row},N_{col})}\right)^{\top}, \qquad i = 0, 1, 2, \ldots.$$

This vector is random because Equations 1–9 involve the uncertain (random) coefficients $E_{max}(t)$ and $T_{max}(t)$.

The soil-moisture sensor network comprises N_{sen} sensors placed at locations $\mathbf{x}_l$ ($l = 1, \ldots, N_{sen}$) throughout the soil domain Ω. With sampling frequency $1/\Delta t_{obs}$, the lth sensor takes N_{obs} measurements of the volumetric soil water content, θ_l^k, at the observation times t_k ($k = 1, \ldots, N_{obs}$). The difference between the observation θ_l^k and the true value of the water content, $\tilde{\theta}(\mathbf{x}_l, t_k)$, is due to a random measurement error ϵ_l^k:

$$\theta_l^k = \tilde{\theta}(\mathbf{x}_l, t_k) + \epsilon_l^k, \qquad l = 1, \ldots, N_{sen}, \quad k = 1, \ldots, N_{obs}. \tag{11}$$

At each measurement time, the observations in Equation 11 form the N_{sen}-dimensional data vector $\mathbf{d}^k = \left\{\theta_l^k : l = 1, \ldots, N_{sen}\right\}$, for $k = 1, \ldots, N_{obs}$. We model the errors ϵ_l^k as zero-mean (bias-free) Gaussian white noise, such that $\mathbb{E}\left\{\epsilon_l^k\right\} = 0$ and $\mathbb{E}\left\{\epsilon_l^k \epsilon_\nu^\mu\right\} = \sigma^2 \delta_{l\nu} \delta_{k\mu}$ ($l, \nu = 1, \ldots, N_{sen}$ and $k, \mu = 1, \ldots, N_{obs}$), where $\mathbb{E}\{\cdot\}$ denotes the ensemble average, σ^2 is the variance (strength) of the white noise, and δ_{ij} is the Kronecker delta. Therefore, the data vector $\mathbf{d}^k$ is characterized by the multivariate Gaussian probability density function (PDF)

$$f_{\mathbf{d}}(\mathbf{d}; t_k) = \frac{1}{(2\pi)^{N_{el}/2} |\boldsymbol{\Sigma}_{\mathbf{d}}|^{1/2}} \exp\left[-\frac{1}{2}\left(\mathbf{d} - \bar{\mathbf{d}}^k\right)^{\top} \boldsymbol{\Sigma}_{\mathbf{d}}^{-1} \left(\mathbf{d} - \bar{\mathbf{d}}^k\right)\right] \tag{12}$$

with mean $\bar{\mathbf{d}}^k$ and covariance matrix $\boldsymbol{\Sigma}_{\mathbf{d}}$. The off-diagonal terms of the latter are all 0, and the diagonal terms are σ^2.

As mentioned earlier, the length N_{el} of the solution vector $\boldsymbol{\theta}(\tau_i)$ differs from the length N_{sen} of the data vector $\mathbf{d}^k$, and $\boldsymbol{\theta}(\tau_i)$ is computed at discrete times τ_i of which the observation times t_k are a subset. To facilitate the comparison between the model prediction $\boldsymbol{\theta}$ and the observations $\mathbf{d}$, it is common to introduce the $N_{sen} \times N_{el}$ observational matrix $\mathbf{H}_{obs}^k$. Thus, the operation $\mathbf{H}_{obs}^k \boldsymbol{\theta}$ extracts those elements of the N_{el}-dimensional solution vector $\boldsymbol{\theta}^\star$ that match the locations (elements) and times of the N_{sen}-dimensional observation vector $\mathbf{d}^k$.

Since we have assumed Equations 1–9 to provide the error-free representation of reality, their solution $\theta(\mathbf{x}, t)$ coincides with the true water content $\tilde{\theta}(\mathbf{x}, t)$ as long as all the model parameters are known with certainty. This assumption can be relaxed by adding the model error, typically a space-time white noise, to Equation 1; this noise would account for a possible discrepancy between $\theta(\mathbf{x}, t)$ and $\tilde{\theta}(\mathbf{x}, t)$ due to the breakdown of the modeling assumptions.

3. Alternative Strategies for ET Estimation

3.1. Data-Driven Estimation of Total ET

The total ET rate (m/hr), $S_{tot}(t)$, is computed from its spatially distributed counterpart in Equation 10 via integration,

$$S_{\text{tot}}(t) = \frac{1}{L_x}\int_{\Omega} T(\mathbf{x}, t, \theta(\mathbf{x}, t))\mathrm{d}\mathbf{x} + \frac{1}{L_x}\int_0^{L_x} E(x, t, \theta(x, 0, t))\mathrm{d}x, \tag{13}$$

or via a numerical approximation of these integrals. To simplify the presentation, we suppose that the soil-moisture sensors are equally spaced. The soil-water balance approach (Breña Naranjo et al., 2011; Vrugt, van Wijk, et al., 2001; Wilson et al., 2001) for the estimation of the total ET $S^k_{\text{tot}} = S_{\text{tot}}(t_k)$ at discrete observation times t_k consists of the following two steps. First, the soil domain Ω is discretized with a uniform mesh, whose rectangular elements have lengths Δx_{obs} and Δz_{obs} in the x and z directions, respectively. The values of Δx_{obs} and Δz_{obs} are chosen such that each element contains a single sensor; in a typical simulation, $\Delta z \ll \Delta z_{\text{obs}}$, $\Delta x \ll \Delta x_{\text{obs}}$, and $\Delta t \ll \Delta t_{\text{obs}}$. Without loss of generality, we assume Δz_{obs}, Δx_{obs}, and Δt_{obs} to be the integer multiples of their respective numerical-mesh counterparts. This observational mesh comprises N_{sen} elements, which are arranged in $N^{\text{row}}_{\text{sen}}$ rows and $N^{\text{col}}_{\text{sen}}$ columns, such that $N_{\text{sen}} = N^{\text{row}}_{\text{sen}} \cdot N^{\text{col}}_{\text{sen}}$. Second, S^k_{tot} is related to the prescribed flow rate $P^k = P(t_k)$ of the dripping device and to the observed soil moisture $\mathbf{d}^k = \left\{\theta^k_1, \ldots, \theta^k_{N_{\text{sen}}}\right\}$ by water balance (Vrugt, van Wijk, et al., 2001),

$$S^k_{\text{tot}} = \frac{P^k N_{\text{d}} L_{\text{d}}}{L_x} - \sum_{l=1}^{N_{\text{sen}}} \frac{\theta^k_l - \theta^{k-1}_l}{\Delta t_{\text{obs}} L_x}\Delta z_{\text{obs}}\Delta x_{\text{obs}}, \qquad k = 1, \ldots, N_{\text{obs}}. \tag{14}$$

Since this strategy makes no use of the Richards equation, it is as good as the available data $\mathbf{d}^k$ (in terms of both quantity and quality). Equally important, it provides no information about the spatial variability of ET.

DA enables one to augment this data-driven approach with model predictions. To this end, we replace the data $\mathbf{d}^k$ in Equation 14 with the corresponding model predictions $\theta(\mathbf{x}_l, \tau_k)$ obtained by Equations 1–9 with uncertain $E_{\max}(t)$ and $T_{\max}(t)$,

$$S^k_{\text{tot}} = \frac{P^k N_{\text{d}} L_{\text{d}}}{L_x} - \sum_{l=1}^{N_{\text{el}}} \frac{\theta(\mathbf{x}_l, t_k) - \theta(\mathbf{x}_l, t_{k-1})}{\Delta t_{\text{obs}} L_x}\Delta z\Delta x. \tag{15}$$

The direct application of EnKF (Pan & Wood, 2006; Reichle et al., 2008) starts by updating the (mean and variance of) model predictions $\theta(\mathbf{x}_l, \tau_k)$ on the data $\mathbf{d}^k$ and then uses Equation 15 to compute S^k_{tot}. The statistics of $\theta(\mathbf{x}_l, \tau_k)$ are obtained by solving the flow problem in Equations 1–9 multiple times, for many realizations of the random inputs $E_{\max}(t)$ and $T_{\max}(t)$. Consequently, this procedure can become prohibitively expensive, especially for high-dimensional problems.

3.2. Model-Informed Observables for ET Estimation

To overcome these drawbacks, we extend the 1D strategy of Li et al. (2021) to higher spatial dimensions. This strategy treats ET rate, $S(\mathbf{x}, t)$ in Equation 10, as a state variable to be updated directly. In the discretized form, the soil surface ($z = 0$) in Equation 10 is represented by the first row of elements, and $E \equiv 0$ in the remaining $(N_{\text{row}} - 1)$ rows; thus, the discretized $S(\mathbf{x}, t)$ forms a vector of length N_{el},

$$\boldsymbol{S}(\tau_i) = \left(S_{(1,1)}, \ldots, S_{(N_{\text{row}},1)}, \ldots, S_{(1,N_{\text{col}})}, \ldots, S_{(N_{\text{row}},N_{\text{col}})}\right)^{\mathsf{T}}.$$

We denote by $\theta^\star(\mathbf{x}_l, \tau_i)$ a numerical solution of Equations 1–9 with $E \equiv 0$ and $T \equiv 0$ and the recursive initial condition. For $i = 0$, the initial condition is given by Equation 9 and the system is advanced $N_k = \Delta t_{\text{obs}}/\Delta t$ time steps until the first observation time, t_1, is reached; after that, the posterior mean of $\theta(\mathbf{x}_l, t_1)$, whose computation is detailed below, is used as the initial condition for the next N_k time steps of computing $\theta^\star(\mathbf{x}_l, \tau_i)$ for $i = N_k + 1, \ldots, 2N_k$; etc. Since the uncertain E and T are the only source of randomness in the original flow problem, setting both of them to zero renders $\theta^\star(\mathbf{x}_l, \tau_i)$ deterministic. This solution is written in the vector form,

$$\boldsymbol{\theta}^\star(\tau_i) = \left(\theta^\star_{(1,1)}, \ldots, \theta^\star_{(N_{\text{row}},1)}, \ldots, \theta^\star_{(1,N_{\text{col}})}, \ldots, \theta^\star_{(N^\star_{\text{row}},N_{\text{col}})}\right)^{\mathsf{T}}.$$

Let us assume that the ET rate $S(\cdot, t)$ does not change during the time interval Δt_{obs} between any two adjacent observation times $t_{k-1} = (k-1)\Delta t_{\text{obs}}$ and $t_k = k\Delta t_{\text{obs}}$, for $k = 1, \ldots, N_{\text{obs}}$. Then, the rate of change of the amount

of water in the lth element of the *numerical* mesh, $\mathbf{x}_l$ ($l = 1, \ldots, N_{\text{el}}$), during the kth *observational* time step, $t_k = k\Delta t_{\text{obs}}$ ($k = 1, \ldots, N_{\text{obs}}$), is

$$\frac{\theta_l(t_k) - \theta_l(t_{k-1})}{\Delta t_{\text{obs}} L_x}\Delta z \Delta x = \frac{\theta_l^\star(t_k) - \theta_l(t_{k-1})}{\Delta t_{\text{obs}} L_x}\Delta z \Delta x - \frac{\mathcal{S}_l(t_k)\Delta z \Delta x}{L_x}, \tag{16}$$

where θ_l, $\theta_l^\star$ and $\mathcal{S}_l$ refer to the lth component of the vectors $\boldsymbol{\theta}$, $\boldsymbol{\theta}^\star$ and $\boldsymbol{\mathcal{S}}$, respectively. Rearranging the terms and introducing $S_l(\cdot) \equiv \mathcal{S}_l(\cdot)\Delta z \Delta x / L_x$ yields, in the vector form,

$$\mathbf{S}(t_k) = \frac{\boldsymbol{\theta}^\star(t_k) - \boldsymbol{\theta}(t_k)}{\Delta t_{\text{obs}} L_x}\Delta z \Delta x, \qquad k = 1, \ldots, N_{\text{obs}}. \tag{17}$$

Sections 3.2.1 and 3.2.2 present two alternative DA strategies, EnKF and MLE supplemented with the Fisher information matrix, for the ET estimation from soil-moisture data. Both strategies provide a quantitative measure of uncertainty associated with this estimation.

3.2.1. Ensemble Kalman Filter

A key novelty of our EnKF approach is to replace, in Equation 17, the expensive-to-compute random model predictions $\boldsymbol{\theta}(t_k)$ with the available data $\mathbf{d}^k$. Making use of the observation matrix $\mathbf{H}_{\text{obs}}$, this substitution approximates $\mathbf{S}(t_k)$ with

$$\mathbf{Y}^k = \frac{\mathbf{H}_{\text{obs}}^k \boldsymbol{\theta}^\star - \mathbf{d}^k}{\Delta t_{\text{obs}} L_x}\Delta z \Delta x, \qquad k = 1, \ldots, N_{\text{obs}}. \tag{18}$$

Since $\boldsymbol{\theta}^\star(\cdot)$ is deterministic, $\mathbf{Y}^k$ has the same PDF $f_{\mathbf{Y}^k}(\mathbf{y})$ as the soil-moisture data $\mathbf{d}^k$ or, equivalently, the measurement error $\boldsymbol{\epsilon}(\cdot)$. For the Gaussian white noise $\boldsymbol{\epsilon}(\cdot)$,

$$f_{\mathbf{Y}^k}(\mathbf{y}) = \frac{1}{(2\pi)^{N_{\text{el}}/2}|\boldsymbol{\Sigma}_{\mathbf{Y}}|^{1/2}}\exp\left[-\frac{1}{2}(\mathbf{y} - \boldsymbol{\mu}_{\mathbf{Y}})^\top \boldsymbol{\Sigma}_{\mathbf{Y}}^{-1}(\mathbf{y} - \boldsymbol{\mu}_{\mathbf{Y}})\right], \tag{19}$$

It follows from Equations 11, 17, and 18 that the mean, $\boldsymbol{\mu}_{\mathbf{Y}}(t_k)$, and covariance matrix, $\boldsymbol{\Sigma}_{\mathbf{Y}}(t_k)$, of this PDF are given by

$$\boldsymbol{\mu}_{\mathbf{Y}}(t_k) = \mathbf{H}_{\text{obs}}^k \boldsymbol{\mu}_{\mathbf{S}} \qquad \text{and} \qquad \boldsymbol{\Sigma}_{\mathbf{Y}}(t_k) = \left(\frac{\Delta z \Delta x}{\Delta t_{\text{obs}} L_x}\right)^2 \boldsymbol{\Sigma}_{\mathbf{d}}(t_k). \tag{20}$$

Rather than assimilating the soil-moisture data $\mathbf{d}^k$, we assimilate their rescaled counterpart $\mathbf{Y}^k$.

The solution of Equations 1–9 with uncertain input parameters $T_{\max}^k$ and $E_{\max}^k$ is a multivariate PDF $f_{\mathbf{S}}(\mathbf{s}; t)$. In Bayesian DA, this PDF is referred to as *prior* because it is not informed by the observations $\mathbf{d}^k$. Since $T_{\max}^k$ and $E_{\max}^k$ are constant during $\Delta t_{\text{obs}} = t_k - t_{k-1}$ ($k \geq 1$), we treat them as independent Gaussian variables whose PDFs

$$f_m(\xi_m) = \frac{1}{\sqrt{2\pi}\sigma_m}\exp\left[-\frac{(\xi_m - \mu_m)^2}{2\sigma_m^2}\right], \qquad m = T_{\max}, E_{\max} \tag{21}$$

have respective means $\mu_{T_{\max}}$ and $\mu_{E_{\max}}$ and standard deviations $\sigma_{T_{\max}}$ and $\sigma_{E_{\max}}$. The nonlinearity of Equations 1–9 suggests that the model output, $f_{\mathbf{S}}(\mathbf{s}; t)$, is not guaranteed to be Gaussian, even though the model inputs are (Lu et al., 2002; Tartakovsky, Guadagnini, et al., 2003; Tartakovsky, Lu, et al., 2003; among others). Nevertheless, EnKF assumes the prior $f_{\mathbf{S}}(\mathbf{s}; t_k)$ at observation times t_k to be multivariate Gaussian,

$$f_{\mathbf{S}}(\mathbf{s}; t_k) = \frac{1}{(2\pi)^{N_{\text{el}}/2}|\boldsymbol{\Sigma}_{\mathbf{S}}|^{1/2}}\exp\left[-\frac{1}{2}\left(\mathbf{s} - \boldsymbol{\mu}_{\mathbf{S}}\right)^\top \boldsymbol{\Sigma}_{\mathbf{S}}^{-1}\left(\mathbf{s} - \boldsymbol{\mu}_{\mathbf{S}}\right)\right]. \tag{22}$$

The mean $\boldsymbol{\mu}_{\mathbf{S}}(t_k)$ (a vector of length N_{el}) and covariance $\boldsymbol{\Sigma}_{\mathbf{S}}(t_k)$ (an $N_{\text{el}} \times N_{\text{el}}$ matrix) are approximated by their sample-based counterparts computed as follows. First, N_{sam} samples (realizations) of $T_{\max}$ and $E_{\max}$ are drawn from the Gaussian PDFs in Equation 21. Second, for each of these realizations, solutions of the flow Equations 1–9, $\boldsymbol{\theta}^\star$ and $\boldsymbol{\theta}$, are used in Equation 17 to compute realizations of $\mathbf{S}$. Finally, the resulting N_{sam} samples of $\mathbf{S}$ are processed to evaluate the sample mean $\boldsymbol{\mu}_{\mathbf{S}}$ and the sample covariance matrix $\boldsymbol{\Sigma}_{\mathbf{S}}$.

Algorithm 1. ET Estimation via EnKF

For $k = 1, \ldots, N_{obs}$:
1. Read flow rate $P(t_k)$
2. Solve Equations 1–9 with $E \equiv 0$ and $T \equiv 0$ to obtain $\boldsymbol{\theta}^\star(t_k)$; the initial condition in Equation 9 is given by $\boldsymbol{\theta}_0$ for $k = 1$ and $\boldsymbol{\theta}(t_{k-1})$ for $k \geq 2$
3. Post-process soil moisture data $\mathbf{d}^k$ to compute $\mathbf{y}^k$ via Equation 18
4. For the lth sample ($l = 1, \ldots, N_{sam}$):
(a) Draw realizations of $T^k_{\max}$ and $E^k_{\max}$ from their respective PDFs in Equation 21
(b) Use these values in Equations 4–6 to compute $T(\cdot, t_1)$ and $E(\cdot, t_1)$; functionals $\gamma_T(\theta(\mathbf{x}, t))$ and $\gamma_E(\theta(x, 0, t))$ are evaluated at $\boldsymbol{\theta}_0$ for $k = 1$ and $\boldsymbol{\theta}(t_{k-1})$ for $k \geq 2$
(c) Use Equation 10 to compute the ET rate $S(\mathbf{x}, t_k)$
5. Compute the prior mean $\boldsymbol{\mu}_{\mathbf{S}}(t_k)$ and covariance $\boldsymbol{\Sigma}_{\mathbf{S}}(t_k)$ of $\mathbf{S}(t_k)$ in Equation 22
6. Compute the posterior mean $\hat{\boldsymbol{\mu}}_{\mathbf{S}}(t_k)$ and covariance $\hat{\boldsymbol{\Sigma}}_{\mathbf{S}}(t_k)$ of $\mathbf{S}(t_k)$ in Equations 26 and 27
7. Solve Equations 1–9 with $\mathbf{S} = \hat{\boldsymbol{\mu}}_{\mathbf{S}}(t_k)$ to forecast $\boldsymbol{\theta}(t_k)$

The prior PDF $f_{\mathbf{S}}(\mathbf{s}; t_k)$ is updated on observed values $\mathbf{y}^k$ of the random data $\mathbf{Y}^k$ by means of the Bayes rule,

$$f_{\mathbf{S}|\mathbf{Y}^k=\mathbf{y}^k}(\mathbf{s}; t_k) \sim f_{\mathbf{Y}^k|\mathbf{S}=\mathbf{s}}(\mathbf{s}; \mathbf{y}^k; t_k) f_{\mathbf{S}}(\mathbf{s}; t_k), \tag{23}$$

to obtain the *posterior* PDF $f_{\mathbf{S}|\mathbf{Y}^k=\mathbf{y}^k}(\mathbf{s}; t_k)$; it is the PDF of $\mathbf{S}$ conditioned on the random data $\mathbf{Y}^k$ taking the observed values $\mathbf{y}^k$. The *likelihood* function

$$f_{\mathbf{Y}^k|\mathbf{S}=\mathbf{s}}(\mathbf{s}; \cdot) = \frac{1}{(2\pi)^{N_{el}/2}|\boldsymbol{\Sigma}_{\mathbf{Y}}|^{1/2}} \exp\left[-\frac{1}{2}\left(\mathbf{y}^k - \mathbf{H}^k_{obs}\mathbf{s}\right)^\top \boldsymbol{\Sigma}_{\mathbf{Y}}^{-1}\left(\mathbf{y}^k - \mathbf{H}^k_{obs}\mathbf{s}\right)\right], \tag{24}$$

is constructed by treating as function of $\mathbf{s}$ the PDF of the data $\mathbf{Y}^k$ conditioned on the model predicting the value $\mathbf{s}$ of the state variable $\mathbf{S}$. This conditional Gaussian PDF, $f_{\mathbf{Y}^k|\mathbf{S}=\mathbf{s}}(\mathbf{y}; \mathbf{s}; t_k)$, corresponds to the data model $f_{\mathbf{Y}^k}(\mathbf{y})$ in Equation 19, wherein the model prediction $\mathbf{s}$ replaces the mean of the data, $\bar{\mathbf{d}}^k$. According to Equation 23, this choice of the Gaussian prior (Equation 22) and the Gaussian likelihood function (Equation 24) translates into the Gaussian posterior,

$$f_{\mathbf{S}|\mathbf{Y}}(\mathbf{s}; t_k) = \frac{1}{(2\pi)^{N_{obs}/2}|\hat{\boldsymbol{\Sigma}}_{\mathbf{S}}|^{1/2}} \exp\left[-\frac{1}{2}\left(\mathbf{s} - \hat{\boldsymbol{\mu}}_{\mathbf{S}}\right)^\top \hat{\boldsymbol{\Sigma}}_{\mathbf{S}}^{-1}\left(\mathbf{s} - \hat{\boldsymbol{\mu}}_{\mathbf{S}}\right)\right], \tag{25}$$

whose posterior mean, $\hat{\boldsymbol{\mu}}_{\mathbf{S}}(t_k)$, and covariance, $\hat{\boldsymbol{\Sigma}}_{\mathbf{S}}(t_k)$, are given by

$$\hat{\boldsymbol{\mu}}_{\mathbf{S}} = \boldsymbol{\mu}_{\mathbf{S}} + \mathbf{K}\left(\mathbf{y}^k - \mathbf{H}^k_{obs}\boldsymbol{\mu}_{\mathbf{S}}\right), \qquad \hat{\boldsymbol{\Sigma}}_{\mathbf{S}} = \left(\mathbf{I} - \mathbf{K}\mathbf{H}^k_{obs}\right)\boldsymbol{\Sigma}_{\mathbf{S}}. \tag{26}$$

In this *Kalman update*, $\mathbf{I}$ denotes the $N_{el} \times N_{el}$ identity matrix, and the $N_{el} \times N_{sen}$ matrix

$$\mathbf{K} = \boldsymbol{\Sigma}_{\mathbf{S}}\mathbf{H}^{k^\top}_{obs}\left(\mathbf{H}^k_{obs}\boldsymbol{\Sigma}_{\mathbf{S}}\mathbf{H}^{k^\top}_{obs} + \boldsymbol{\Sigma}_{\mathbf{Y}}\right)^{-1} \tag{27}$$

is referred to as the *Kalman gain*.

Algorithm 1 summarizes the EnKF strategy described above. General considerations allow one to expect this algorithm to significantly outperform the previous versions of EnKF used to estimate ET from soil-moisture data (Li et al., 2021; Pan & Wood, 2006; Reichle et al., 2008) in terms of either accuracy or efficiency or both. Unlike these one-dimensional methods, Algorithm 1 accounts for the horizontal component of the water flux, which is likely to be pronounced in heterogeneous soils subjected to drip irrigation. Algorithm 1 is significantly faster than the EnKF implementations of Pan and Wood (2006) and Reichle et al. (2008), which find it necessary to solve the nonlinear flow problem (Equations 1–9) N_{sam} times, for each ensemble member.

Algorithm 1 shares the shortcomings of other EnKF implementations. To accelerate the full Bayesian update (Boso & Tartakovsky, 2020), the EnKF replaces the probabilistic solution of Equations 1–9 with its multivariate Gaussian counterpart (Equation 22); this foundational step introduces an uncontrollable approximation (Bocquet et al., 2015), whose accuracy has to be verified via numerical experimentation (see Section 4 below). Moreover, the EnKF requires one to specify a reasonable prior for the uncertain parameters, for example, the means and variances of $T_{\max}$ and $E_{\max}$ in Equation 21. For the situations when this information is unavailable, we propose an MLE-based alternative.

3.2.2. Maximum Likelihood Estimator With Fisher Information

MLE is a deterministic technique that ignores (random) measurement errors ($\epsilon_n^k \equiv 0$ in Equation 11). At any observation time t_k, the loss function

$$\tilde{\mathcal{L}}^k = \frac{1}{2N_{\text{sen}}}\tilde{\mathbf{A}}^\top\tilde{\mathbf{A}} \tag{28a}$$

provides a measure of mismatch between the observed, $\mathbf{d}^k$, and predicted, $\boldsymbol{\theta}(t_k)$, water content. Here, $\tilde{\mathbf{A}} = \mathbf{d}^k - \mathbf{H}_{\text{obs}}^k\boldsymbol{\theta}\left(t_k; T_{\max}^k, E_{\max}^k\right)$, and the notation $\boldsymbol{\theta}\left(\cdot; T_{\max}^k, E_{\max}^k\right)$ makes explicit the dependence of the model prediction on uncertain $T_{\max}(t)$ and $E_{\max}(t)$. Making use of the solution $\boldsymbol{\theta}^\star(t)$ introduced above, we rewrite $\tilde{\mathbf{A}}$ as

$$\tilde{\mathbf{A}} = \mathbf{H}_{\text{obs}}^k\left[\boldsymbol{\theta}^\star(t_k) - \boldsymbol{\theta}\left(t_k; T_{\max}^k, E_{\max}^k\right)\right] - \left(\mathbf{H}_{\text{obs}}^k\boldsymbol{\theta}^\star(t_k) - \mathbf{d}^k\right). \tag{28b}$$

Accounting for Equation 17,

$$\mathcal{L}^k = \frac{1}{2N_{\text{sen}}}\mathbf{A}^\top\mathbf{A}, \qquad \mathbf{A} = \mathbf{H}_{\text{obs}}^k\mathbf{S}(t_k) - \frac{\Delta z\Delta x}{\Delta t_{\text{obs}}L_x}\left(\mathbf{H}_{\text{obs}}^k\boldsymbol{\theta}^\star(t_k) - \mathbf{d}^k\right), \tag{29}$$

where $\mathcal{L}^k = \tilde{\mathcal{L}}^k(\Delta z\Delta x)^2/(\Delta t_{\text{obs}}L_x)^2$. The values of $T_{\max}^k$ and $E_{\max}^k$ that minimize $\mathcal{L}^k$ are referred to as their MLEs.

This minimization problem is solved by gradient descent with the components of the gradient computed analytically. For the ET model in Equations 4–6, these components are

$$\frac{\partial\mathcal{L}^k}{\partial T_{\max}^k} = \left[\mathbf{d}^k - \mathbf{H}_{\text{obs}}^k\boldsymbol{\theta}\left(t_k; T_{\max}^k, E_{\max}^k\right)\right]^\top\mathbf{H}_{\text{obs}}^k(\boldsymbol{\gamma}_T\circ\mathbf{F}_{\text{root}}), \tag{30a}$$

$$\frac{\partial\mathcal{L}^k}{\partial E_{\max}^k} = \left[\mathbf{H}_{\text{top}}^k\left(\mathbf{d}^k - \mathbf{H}_{\text{obs}}^k\boldsymbol{\theta}\left(t_k; T_{\max}^k, E_{\max}^k\right)\right)\right]^\top\mathbf{H}_{\text{top}}^k\mathbf{H}_{\text{obs}}^k\boldsymbol{\gamma}_E, \tag{30b}$$

where

$$\begin{aligned}
\mathbf{F}_{\text{root}} &= \left(F_{\text{root}}(x_1, z_1), \ldots, F_{\text{root}}(x_{\text{row}}, z_1), \ldots, F_{\text{root}}(x_1, z_{\text{col}}), \ldots, F_{\text{root}}(x_{\text{row}}, z_{\text{col}})\right)^\top,\\
\boldsymbol{\gamma}_T &= \left(\gamma_T\left(\theta_{(x_1,z_1)}\right), \ldots, \gamma_T\left(\theta_{(x_{\text{row}},z_1)}\right), \ldots, \gamma_T\left(\theta_{(x_1,z_{\text{col}})}\right), \ldots, \gamma_T\left(\theta_{(x_{\text{row}},z_{\text{col}})}\right)\right)^\top,\\
\boldsymbol{\gamma}_E &= \left(\gamma_E\left(\theta_{(x_1,z_1)}\right), \ldots, \gamma_E\left(\theta_{(x_{\text{row}},z_1)}\right), \ldots, \gamma_E\left(\theta_{(x_1,z_{\text{col}})}\right), \ldots, \gamma_T\left(\theta_{(x_{\text{row}},z_{\text{col}})}\right)\right)^\top,
\end{aligned}$$

an $N_{\text{top}} \times N_{\text{sen}}$ matrix $\mathbf{H}_{\text{top}}^k$ extracts the soil water content measured at the soil surface from the data array $\mathbf{d}^k$, N_{top} is the number of sensors placed at the top soil layer, and the symbol $\circ$ denotes the element-wise multiplication. The MLE procedure described above is summarized in Algorithm 2.

For a prescribed tolerance ϵ, Algorithm 2 has converged when

$$\left|\frac{\mathcal{L}_{(\nu)}^k - \mathcal{L}_{(\nu-1)}^k}{\mathcal{L}_{(\nu-1)}^k}\right| \le \epsilon, \qquad \nu = 1, 2, \ldots \tag{31}$$

between two successive iterations ($\nu - 1$ and ν). A suitable choice of the learning rates α_T and α_E accelerates the convergence without overshooting the minimum. We use exponentially decaying learning rates, $\alpha_T = 20{,}000 \cdot (0.9)^{\nu-1}$ and $\alpha_E = 0.05 \cdot (0.8)^{\nu-1}$, and set $\epsilon = 10^{-4}$.

Algorithm 2 yields deterministic estimates of $T_{\max}$ and $E_{\max}$. We use the Fisher information matrix $\boldsymbol{\mathcal{I}}$ quantify the uncertainty inherent in these estimators. We reintroduce the measurement noise into our deterministic MLE

Algorithm 2. ET Estimation via MLE

For k = 1, …, N_{obs}:
1. Read flow rate $P(t_k)$
2. Set $T_{max}^{k,(\nu=0)} = 0$ and $E_{max}^{k,(\nu=0)} = 0$

For ν = 1, 2, … (until convergence):
(a) Compute $T(\mathbf{x}, t_k)$ and $E(\theta(x, 0), t_k)$ via Equations 4–6
(b) Compute $\boldsymbol{\theta}(t_k)$ by solving Equations 1–9; the initial condition in Equation 9 is given by $\boldsymbol{\theta}_0$ for k = 1 and $\boldsymbol{\theta}(t_{k-1})$ for $k \geq 2$
(c) Compute $\mathbf{c}^k = \mathbf{d}^k - \mathbf{H}_{obs}^k \theta\left(t_k; T_{max}^{k,(\nu)}, E_{max}^{k,(\nu)}\right)$
(d) For prescribed learning rates α_T and α_E, update E_{max} according to $E_{max}^{k,(\nu)} = E_{max}^{k,(\nu-1)} - \frac{\alpha_E \Delta z \Delta x^2}{\Delta t_{obs} L_x^2 N_{sen}} \left(\mathbf{H}_{top}^k \mathbf{c}^k\right)^\top \mathbf{H}_{top}^k \mathbf{H}_{obs}^k \boldsymbol{\gamma}_E$
(e) Compute $E(\theta(x, 0), t_k)$ via Equation 6
(f) Compute $\boldsymbol{\theta}(t_k)$ by solving Equations 1–9 with the updated E_{max}; the initial condition in Equation 9 is given by $\boldsymbol{\theta}_0$ for k = 1 and $\boldsymbol{\theta}(t_{k-1})$ for $k \geq 2$
(g) Recompute $\mathbf{c}^k = \mathbf{d}^k - \mathbf{H}_{obs}^k \theta\left(t_k; T_{max}^{k,(\nu)}, E_{max}^{k,(\nu)}\right)$
(h) Update T_{max} according to $T_{max}^{k,(\nu)} = T_{max}^{k,(\nu-1)} - \frac{\alpha_T (\Delta z \Delta x)^2}{\Delta t_{obs} L_x N_{sen}} \left(\mathbf{c}^k\right)^\top \mathbf{H}_{obs}^k (\boldsymbol{\gamma}_T \circ \mathbf{F}_{root})$
(i) Compute $T(\mathbf{x}, t_k)$ via Equation 4 using the updated T_{max}
(j) Compute $\boldsymbol{\theta}(t_k)$ by solving Equations 1–9 with the updated $E(\theta(x, 0), t_k)$ and $T(\mathbf{x}, t_k)$; the initial condition in Equation 9 is given by $\boldsymbol{\theta}_0$ for k = 1 and $\boldsymbol{\theta}(t_{k-1})$ for $k \geq 2$
(k) Compute the loss function $\mathcal{L}_{(\nu)}^k$ via Equation 29

algorithm. Since the noise has zero mean and is Gaussian, and since MLE treats the deterministic flow model (Equations 1–9) as the perfect representation of reality, the ensemble mean of $\mathbf{d}^k$ coincides with the model prediction at the corresponding locations, $\mathbb{E}\{\mathbf{d}^k\} = \mathbf{H}_{obs}^k \theta(t_k)$, and the PDF of $\mathbf{d}^k$ conditioned on the model solution being $\boldsymbol{\theta}(t_k)$ is multivariate Gaussian. The natural logarithm of this conditional PDF is

$$\ln f_{\mathbf{d}|\theta} = C - \frac{1}{2}\left(\mathbf{d}^k - \mathbf{H}_{obs}^k \theta(t_k)\right)^\top \boldsymbol{\Sigma}_{\mathbf{d}}^{-1} \left(\mathbf{d}^k - \mathbf{H}_{obs}^k \theta(t_k)\right), \tag{32}$$

where C is the normalizing constant. In analogy with Equation 29, we rewrite this as

$$\ln f_{\mathbf{d}|\theta} = C - \frac{1}{2}\mathbf{A}^\top \boldsymbol{\Sigma}_{\mathbf{Y}}^{-1} \mathbf{A}. \tag{33}$$

The Hessian matrix

$$\boldsymbol{\mathcal{H}} = \begin{bmatrix} \frac{\partial^2 \ln f_{\mathbf{d}|\theta}}{\partial T_{max}^2} & \frac{\partial^2 \ln f_{\mathbf{d}|\theta}}{\partial T_{max} \partial E_{max}} \\ \frac{\partial^2 \ln f_{\mathbf{d}|\theta}}{\partial E_{max} \partial T_{max}} & \frac{\partial^2 \ln f_{\mathbf{d}|\theta}}{\partial E_{max}^2} \end{bmatrix} \tag{34a}$$

is computed analytically, such that

$$\mathcal{H}_{11} = -(\Delta x \Delta z)^2 \left[\mathbf{H}_{obs}^k (\boldsymbol{\gamma}_T \circ \mathbf{F}_{root})\right]^\top \boldsymbol{\Sigma}_{\mathbf{Y}}^{-1} \left[\mathbf{H}_{obs}^k (\boldsymbol{\gamma}_T \circ \mathbf{F}_{root})\right] \tag{34b}$$

$$\mathcal{H}_{12} = -(\Delta x)^2 \Delta z / L_x \left[\mathbf{H}_{obs}^k (\boldsymbol{\gamma}_T \circ \mathbf{F}_{root})\right]^\top \boldsymbol{\Sigma}_{\mathbf{Y}}^{-1} \left[\mathbf{H}_{top}^k \mathbf{H}_{obs}^k \boldsymbol{\gamma}_E\right] \tag{34c}$$

$$\mathcal{H}_{21} = -(\Delta x)^2 \Delta z / L_x \left[\mathbf{H}_{top}^k \mathbf{H}_{obs}^k \boldsymbol{\gamma}_E\right]^\top \boldsymbol{\Sigma}_{\mathbf{Y}}^{-1} \left[\mathbf{H}_{obs}^k (\boldsymbol{\gamma}_T \circ \mathbf{F}_{root})\right] \tag{34d}$$

$$\mathcal{H}_{22} = -(\Delta x / L_x)^2 \left[\mathbf{H}_{top}^k \mathbf{H}_{obs}^k \boldsymbol{\gamma}_E\right]^\top \boldsymbol{\Sigma}_{\mathbf{Y}}^{-1} \left[\mathbf{H}_{top}^k \mathbf{H}_{obs}^k \boldsymbol{\gamma}_E\right]. \tag{34e}$$

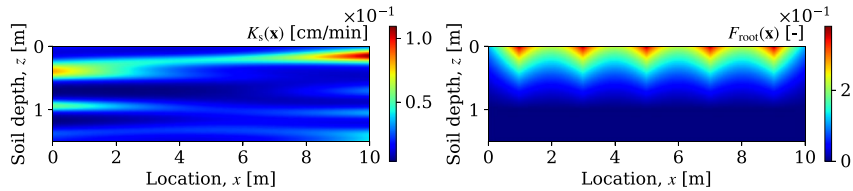

Figure 1. Isotropic saturated hydraulic conductivity $K_s(\mathbf{x})$ (Left) and the normalized root density $F_{root}(\mathbf{x})$ (Right).

If one treats T_{max} and E_{max} as random variables, then the ensemble mean of $\boldsymbol{\mathcal{H}}$ is the information matrix (Lehmann & Casella, 1998),

$$\boldsymbol{\mathcal{I}} = -\mathbb{E}[\boldsymbol{\mathcal{H}}]. \tag{35}$$

Its inverse is the variance-covariance matrix of MLEs of T_{max} and E_{max} (Efron & Hinkley, 1978),

$$\boldsymbol{\mathcal{I}}^{-1} = \begin{bmatrix} \mathrm{var}(T_{max}) & \mathrm{cov}(T_{max}, E_{max}) \\ \mathrm{cov}(E_{max}, T_{max}) & \mathrm{var}(E_{max}) \end{bmatrix}. \tag{36}$$

4. Synthetic Experiments

We consider rows of plants, whose irrigation is such that the soil moisture is spatially uniform in the directions of the rows. The resulting two-dimensional flow domain is 10 m in width (the x coordinate) and 1.5 m in depth (the z coordinate). The plants and dripping devices are located at $x = 1$, 3, 5, 7, and 9 m. A normalized root density, $F_{root}(\mathbf{x})$, is shown in Figure 1, accompanied by a map of saturated hydraulic conductivity $K_s(\mathbf{x})$; Table 1 contains values of the remaining hydraulic properties of the soil and parameters of the root density function in Equations 1–9. Dripping irrigation occurs at 24, 74, 124, and 174 hr; each watering cycle lasts for 4 hr; and each irrigation device has length $L_d = 0.05$ m and operates with flow rate $P(t) = 0.8$ m/hr.

The heterogeneous $K_s(\mathbf{x})$ in Figure 1 is a realization from a log-normal distribution with mean -3.58 and variance 0.89 (Wang & Tartakovsky, 2011) and correlation length 1 m. The ground-truth values of water content $\tilde{\boldsymbol{\theta}}(t)$, ET $\tilde{\mathbf{S}}(t)$, and the total ET rate $\tilde{S}_{tot}(t)$ in Figure 4a are generated by solving Equations 1–9 for given time series $T_{max}(t)$ and $E_{max} = 4.17 \times 10^{-4}$ m/hr. The numerical solution was obtained with the PFLOTRAN code, for the flow

Table 1
Hydraulic Soil Properties, Root Water Uptake Parameters and Initial Guesses for the Statistics of Unknown T_{max} and E_{max}

Parameter	Symbol	Value	Units
Porosity	ϕ	0.4	–
Irreducible water content	θ_i	0.05	–
Field capacity	θ_p	0.4	–
Shape factor in van Genuchten model	α_{vG}	$1 \cdot 10^{-3}$	–
Shape factor in van Genuchten model	m_{vG}	0.5	–
Saturation at the wilting point	θ_w	0.1	–
Saturation at the point of stomatal closure	θ^*	0.2	–
Hygroscopic saturation	θ_h	0.05	–
Initial soil moisture content	θ_0	0.1483	–
Maximum rooting depth in the z direction	z_m	1	m
Horizontal location of maximum root water uptake	x_m	1	m
Prior mean of T_{max}	$\mu_{T_{max}}$	$2 \cdot 10^{-3}$	m/hr
Prior std of T_{max}	$\sigma_{T_{max}}$	$1 \cdot 10^{-3}$	m/hr
Prior mean of E_{max}	$\mu_{E_{max}}$	$4.17 \cdot 10^{-4}$	m/hr
Prior std of E_{max}	$\sigma_{E_{max}}$	$2 \cdot 10^{-4}$	m/hr

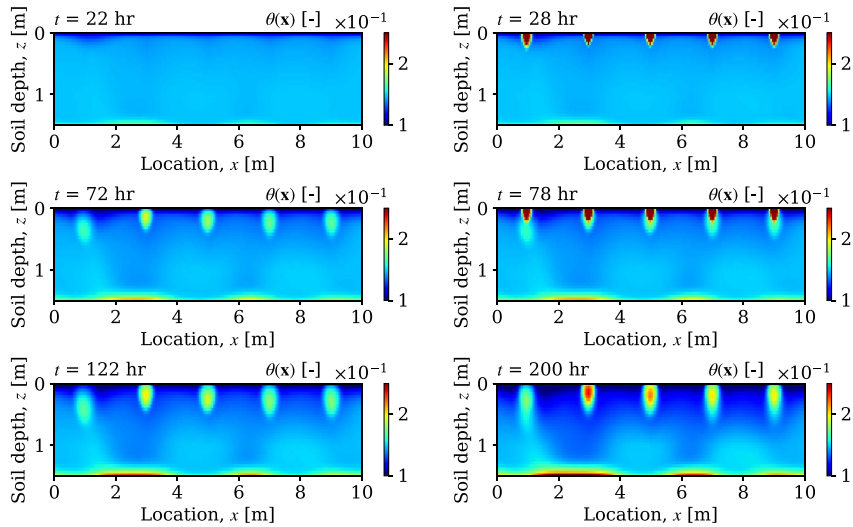

Figure 2. Temporal snapshots of the ground-truth spatial distribution of water content, $\tilde{\theta}(\mathbf{x}, t)$, obtained as a numerical solution of Equations 1–9 with known input parameters.

domain discretized into $N_{el} = 30 \times 200$ square elements of size $\Delta x = \Delta z = 0.05$ m, and the simulated time horizon of 200 hr discretized with time steps $\Delta t = 0.02$ hr.

Figure 2 shows temporal snapshots of the ground-truth maps $\tilde{\boldsymbol{\theta}}(t_k)$. At $t = 28$ and 78 hr, soil saturation in the drippers' vicinity increases dramatically after water application; subsequent water redistribution gradually takes place throughout the soil. At the end of simulation time, $t = 200$ hr, water content $\tilde{\theta}(\mathbf{x}, \cdot)$ exhibits considerable spatial variability in the horizontal direction, reflecting soil heterogeneity. Although not shown here, and as to be expected, we found ET $\tilde{S}(\mathbf{x}, t)$ to be largest close to the soil surface due to evaporation and relatively large root density. Different patters of $\tilde{S}(\mathbf{x}, \cdot)$ for different plants reflect the non-uniformity of $\tilde{\theta}(\mathbf{x}, \cdot)$ through the water-stress response functions $\gamma_T(\theta)$ and $\gamma_E(\theta)$.

A network of $N_{sen} = 10 \times 6$ soil-moisture sensors collects measurements over the time interval of 200 hr with time step $\Delta t_{obs} = 2$ hr. The spatial coordinates (in cm) of these sensors are (x_n, z_m), with $x_n = 100(n-1) + 2.5$ for $n = 1, \ldots, 10$ and $\{z_1, \ldots, z_6\} = \{2.5, 7.5, 12.5, 17.5, 32.5, 97.5\}$. The measurements $\mathbf{d}^k = \left\{\theta_1^k, \ldots, \theta_{N_{sen}}^k\right\}$ at observation times t_k ($k = 1, \ldots, N_{obs} = 100$) are generated, in accordance with the data model in Equation 11, by adding zero-mean white noise ϵ (with $\sigma_\epsilon = 0.001$) to the ground-truth prediction of water content, $\tilde{\theta}$, in Figure 2.

5. Results

We deploy our EnKF and MLE algorithms to infer ET $S(\mathbf{x}, t)$ and total ET rate $S_{tot}(t)$ from the soil-moisture data generated in the previous section. (EnKF comprised 200 ensemble members and used the prior statistics of parameters $T_{max}(t)$ and $E_{max}(t)$ from Table 1.) Figure 3 exhibits temporal snapshots of the spatial maps of $S(\mathbf{x}, t)$ estimated via EnKF. Since their counterparts obtained via MLE are visually similar, we do not show them here; instead, Figure 3 also provides the RMSE $\mathcal{E}(t)$ and the total RMSE $\mathcal{E}_{tot}$,

$$\mathcal{E}(t_k) = \sqrt{\frac{1}{N_{el}} \sum_{i=1}^{N_{el}} \left(\tilde{\mathcal{V}}_i^k - \mathcal{V}_i^k\right)^2}, \qquad \mathcal{E}_{tot} = \sqrt{\frac{1}{N_{obs}} \sum_{k=1}^{N_{obs}} \mathcal{E}(t_k)}, \qquad \mathcal{V} = S \text{ or } \theta, \tag{37}$$

for the two algorithms. Here, $\tilde{\mathcal{V}}_i^k = \tilde{\mathcal{V}}(\mathbf{x}_i, t_k)$ and $\mathcal{V}_i^k = \mathcal{V}(\mathbf{x}_i, t_k)$ are the true and estimated values of the quantity $\mathcal{V}$, which stands for either ET S or water content θ. By these metrics, the EnKF and MLE predictions of ET, $S(\mathbf{x}, t)$, are equally accurate, with EnKF having a slight edge.

Figure 4 shows predictions of the total ET rate, $S_{tot}(t)$, obtained via EnKF and MLE. The initial guess about $S_{tot}(t)$ is, by design, significantly off the mark; not only the true values of the total ET, $\tilde{S}_{tot}(t)$, differ from their prior estimates, they also lie outside the confidence interval, which is made wide to reflect the significant uncertainty

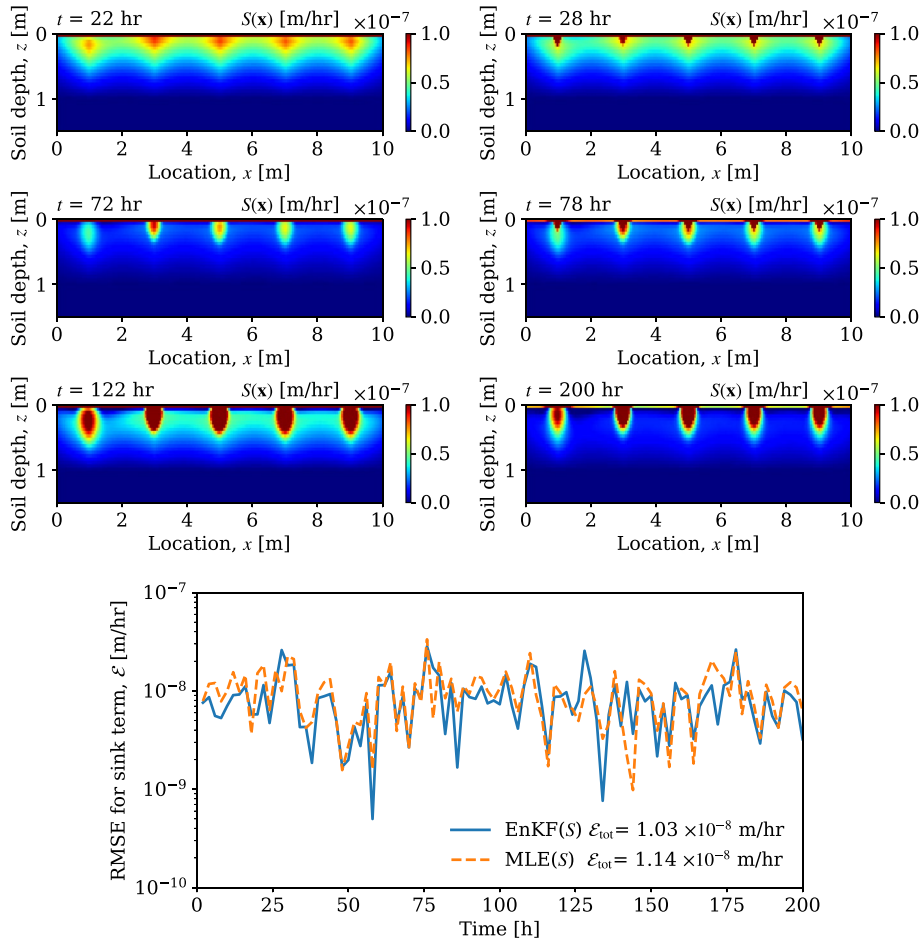

Figure 3. Temporal snapshots of evapotranspiration, $S(\mathbf{x}, t)$, estimated with ensemble Kalman filter (EnKF). The bottom graph shows the root mean square errors, $\mathcal{E}(t)$ and $\mathcal{E}_{\text{tot}}$, for the $S(\mathbf{x}, t)$ estimates obtained, alternatively, via EnKF and maximum likelihood estimation.

in the absence of data. Both EnKF and MLE yield accurate estimates $S_{\text{tot}}(t)$, with MLE significantly underestimating the predictive uncertainty: the true values, $\tilde{S}_{\text{tot}}(t)$, often fall outside the confidence interval resulting from the Fisher information. A more quantitative assessment of the relative accuracy of the EnKF and MLE predictions of $S_{\text{tot}}(t)$ is provided by the relative bias b, the correlation coefficient R, and the relative measure RV,

$$b = \frac{\langle S_{\text{tot}} \rangle - \langle \tilde{S}_{\text{tot}} \rangle}{\langle \tilde{S}_{\text{tot}} \rangle}, \qquad R = \frac{\text{cov}\left(S_{\text{tot}}, \tilde{S}_{\text{tot}}\right)}{\sigma_{S_{\text{tot}}} \sigma_{\tilde{S}_{\text{tot}}}}, \qquad RV = \frac{\sigma_{S_{\text{tot}}}}{\sigma_{\tilde{S}_{\text{tot}}}}, \tag{38}$$

where $\langle \cdot \rangle$, $\text{cov}(\cdot, \cdot)$, and σ indicate the mean, covariance, and standard deviation, respectively. By all these metrics, whose values are reported in Figure 4, EnKF slightly outperforms MLE (recall that an accurate estimate corresponds to b close to 0, and to R and RV close to 1).

Figure 5 shows the EnKF-based predictions of the spatiotemporal evolution of water content, $\theta(\mathbf{x}, t)$. In lieu of the MLE predictors, which are visually similar to those obtained via EnKF, this figure displays the RMSEs for the two methods. Both DA strategies accurately capture the water-redistribution dynamics in the heterogeneous soil, having RMSEs on the order of 10^{-3}. At later times, the RMSE of the MLE-based predictions is slightly smaller than that of its EnKF-based counterpart. The total error of both methods, $\mathcal{E}_{\text{tot}}$, is on the order of 10^{-4}, indicating their ability to accurately predict the water content $\theta(\mathbf{x}, t)$ at unsampled locations.

Finally, we investigate the computational efficiency of our EnKF and MLE algorithms, both relative to each other and in comparison with the standard EnKF that updates water content, EnKF(θ). The computational cost of the MLE algorithm is largely controlled by the cost of an iterative solution of the minimization problem in

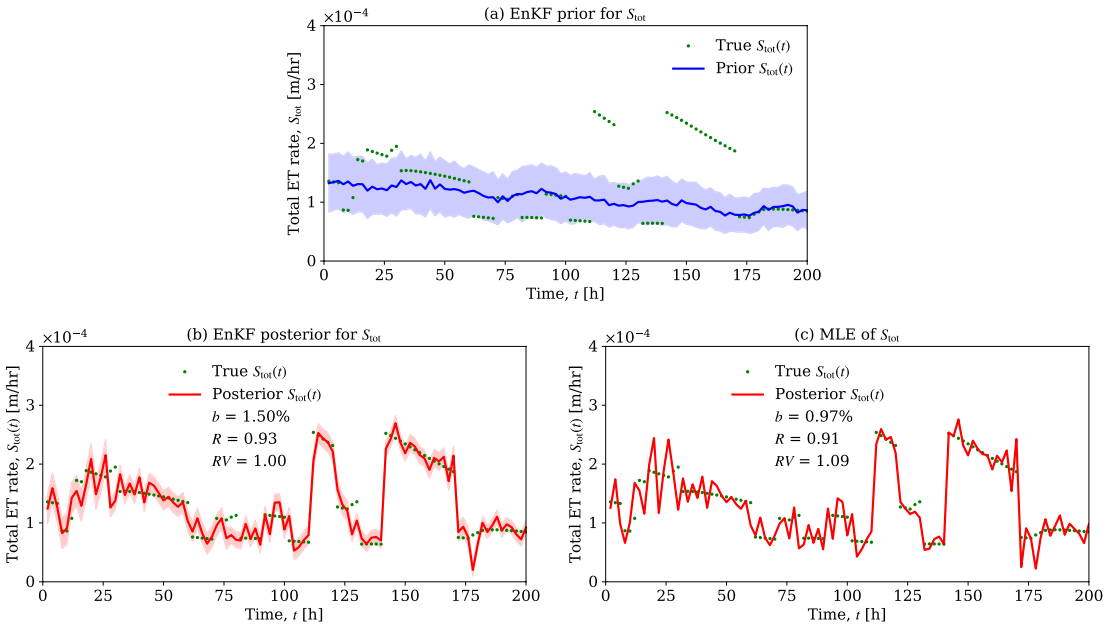

Figure 4. (a) Prior information (guess) about the mean (solid line) and confidence interval (±standard deviation, shaded band) of the total evapotranspiration rate, $S_{tot}(t)$; and the predictions of $S_{tot}(t)$ obtained via, (b) ensemble Kalman filter and (c) maximum likelihood estimation. Both predictions (solid lines) are accompanied by the confidence intervals (shaded bands), even though the MLE-derived standard deviations are too small to be visible. In all plots, the dots indicate the true values of S_{tot}.

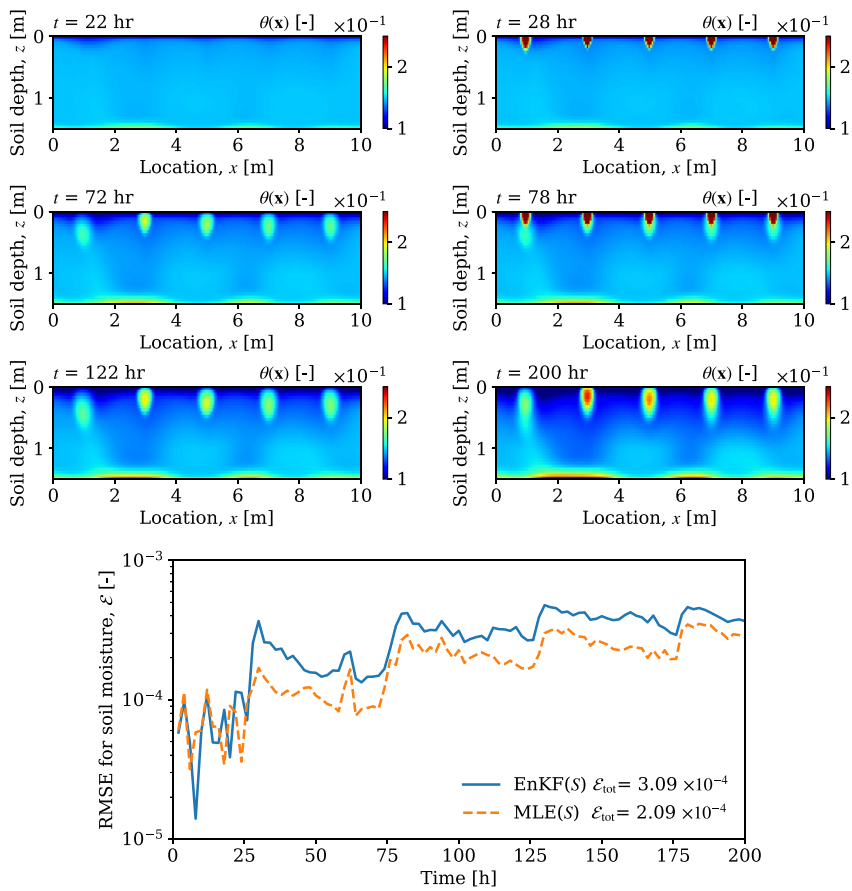

Figure 5. Temporal snapshots of water content, $\theta(\mathbf{x}, t)$, estimated with ensemble Kalman filter (EnKF). The bottom graph shows the root mean square errors, $\mathcal{E}(t)$ and $\mathcal{E}_{tot}$, for the $\theta(\mathbf{x}, t)$ estimates obtained, alternatively, via EnKF and maximum likelihood estimation.

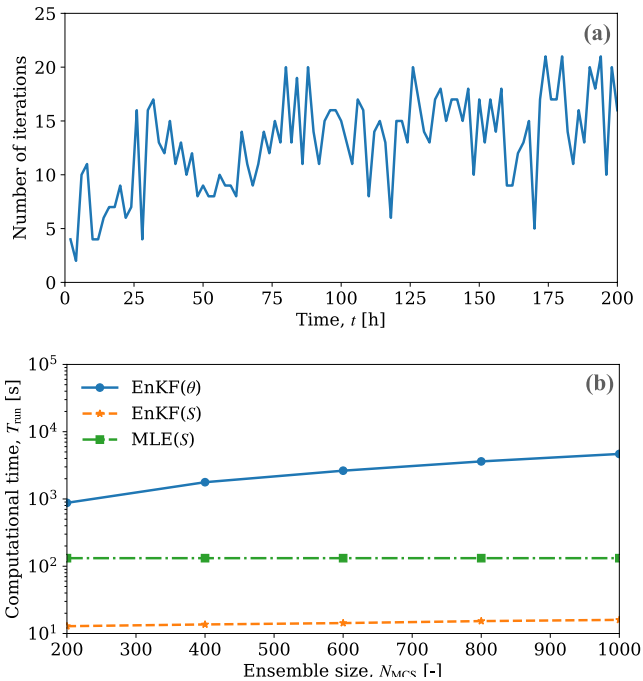

Figure 6. (a) The number of iterations it takes the maximum likelihood estimation (MLE) algorithm to convergence, as function of time t; and (b) computational time per observation time step of ensemble Kalman filter and EnKF(θ), as function of ensemble size N_{sam}. The computational time of MLE is also plotted for comparison, even though it does not depend on N_{sam}.

Equation 30. Figure 6 exhibits the number of iterations at convergence (i.e., when the loss function reaches its minimum within prescribed tolerance) at different observation times. It reveals that our MLE procedure requires on average 13 iterations to converge at all time steps. Given its high precision (Figures 3–5), this makes MLE a viable tool for estimation of the root water uptake profiles and evaporation rates in the absence of the prior knowledge about the parameters $T_{max}(t)$ and $E_{max}(t)$.

Figure 6 also provides a comparison of the computational costs per observation of our EnKF implementation (denoted by EnKF) and of EnKF(θ). As expected, the simulation times of both models increases with the number of ensemble members, N_{sam}. While N_{sam} affects the cost of our implementation only slightly, the computational time of EnKF(θ) grows nearly exponentially with N_{sam}; that is because EnKF(θ) solves the 2D Richards equation for each ensemble member. Since the MLE algorithm does not involve an ensemble of realizations, for comparison purpose, we plot the average computation time of MLE over the total observation time period. To sum up, our EnKF and MLE algorithms are significantly more efficient than EnKF(θ), with EnKF being around two orders of magnitude faster than EnKF(θ) and MLE being around one order of magnitude faster than EnKF, even when $N_{sam} = 200$.

6. Conclusions

We proposed two alternative DA methods, EnKF and MLE, to infer ET rates and root water uptake profiles from a network of soil-moisture sensors placed in a heterogeneous soil. Our numerical experiments mimic drip irrigation of rows of plants with a non-uniform root density distribution. These experiments served to assess the prediction accuracy and computational efficiency of both methods relative to each other and vis-à-vis EnKF(θ), the standard implementation of EnKF that updates the model predictions of water content. Our analysis leads to the following major conclusions.

- Soil heterogeneity, spatial variability of root density, and irrigation practices (e.g., drip irrigation) used in smart agriculture result in complex flow patterns that preclude the one-dimensional treatments underpinning the current DA techniques for ET estimation.
- Our EnKF and MLE algorithms provide accurate predictions of the total ET rate and spatiotemporal varying root water uptake, in the presence of considerable horizontal flow component.
- Our EnKF and MLE algorithms are significantly more efficient than EnKF(θ), with EnKF being around two orders of magnitude faster than EnKF(θ) and MLE being around one order of magnitude faster than EnKF(θ).
- The adoption of exponentially decaying learning rates in the MLE accelerates the computation by at least one order of magnitude in comparison with the MLE with constant learning rates used, for example, by Li et al. (2021).
- The performance of EnKF hinges on the availability of an adequate initial guess of, expert opinion about, the model parameters T_{max} and E_{max}. In the absence of this information, MLE supplemented with the Fisher information should be used.
- The computational efficiency of our EnKF and MLE algorithms facilitates their deployment as a design tool for smart agriculture, for example, to optimize irrigation schedule and/or placement of drippers and sensors.

Even though our inverse modeling methods provide fast and accurate estimations of ET, a large amount of computational time is still consumed by solving the multi-dimensional Richards equation. One way to further accelerate this procedure is to treat a heterogeneous soil as a collection of one-dimensional isolated flow tubes (Sinsbeck & Tartakovsky, 2015; Wang & Tartakovsky, 2011), in a manner consistent with the Dagan-Bresler parameterization (Dagan & Bresler, 1983).

Data Availability Statement

There are no data sharing issues since all of the numerical information is provided in the figures produced by solving the equations in the paper.

Acknowledgments
This research is supported in part by Air Force Office of Scientific Research under award FA9550-21-1-0381 and by National Science Foundation grant EAR-2100927.

References

Anderson, R. G. (2019). *Irrigation in California: Overview and relation to energy*. US Salinity Laboratory.

Ban, Z., Vimal, S., Bhattachan, A., Cucchi, K., Hoover, C., Skaff, N., et al. (2018). Assessing inundation in the Central Valley, CA and its implications for West Nile Virus transmission using remote sensing and hydrological modeling. In *Agu fall meeting abstracts* (Vol. 2018, p. GH31A–08).

Bocquet, M., Raanes, P. N., & Hannart, A. (2015). Expanding the validity of the ensemble Kalman filter without the intrinsic need for inflation. *Nonlinear Processes in Geophysics*, *22*(6), 645–662. https://doi.org/10.5194/npg-22-645-2015

Boso, F., & Tartakovsky, D. M. (2020). Learning on dynamic statistical manifolds. *Proceedings of the Royal Society A*, *476*(2239), 20200213. https://doi.org/10.1098/rspa.2020.0213

Boso, F., & Tartakovsky, D. M. (2022). Information geometry of physics-informed statistical manifolds and its use in data assimilation. *Journal of Computational Physics*, *467*, 111438. https://doi.org/10.1016/j.jcp.2022.111438

Breña Naranjo, J. A., Weiler, M., & Stahl, K. (2011). Sensitivity of a data-driven soil water balance model to estimate summer evapotranspiration along a forest chronosequence. *Hydrology and Earth System Sciences*, *15*(11), 3461–3473. https://doi.org/10.5194/hess-15-3461-2011

Dagan, G., & Bresler, E. (1983). Unsaturated flow in spatially variable fields: 1. Derivation of models of infiltration and redistribution. *Water Resources Research*, *19*(2), 413–420. https://doi.org/10.1029/wr019i002p00413

do Nascimento, F. A. L., da Silva, A. J. P., de Freitas, F. T. O., & dos Anjos Veimrober Junior, L. A. (2021). Sensor placement in 2D/3D wetting patterns from drip irrigation for quantification of evapotranspiration. *Computers and Electronics in Agriculture*, *188*, 106356. https://doi.org/10.1016/j.compag.2021.106356

Efron, B., & Hinkley, D. V. (1978). Assessing the accuracy of the maximum likelihood estimator: Observed versus expected Fisher information. *Biometrika*, *68*(3), 467–487. https://doi.org/10.1093/biomet/65.3.457

Galleguillos, M., Jacob, F., Prevot, L., Faúndez, C., & Bsaibes, A. (2017). Estimation of actual evapotranspiration over a rainfed vineyard using a 1-D water transfer model: A case study within a Mediterranean watershed. *Agricultural Water Management*, *184*, 67–76. https://doi.org/10.1016/j.agwat.2017.01.006

Guswa, A. J., Celia, M. A., & Rodriguez-Iturbe, I. (2002). Models of soil moisture dynamics in ecohydrology: A comparative study. *Water Resources Research*, *38*(9), 5-1–5-15. https://doi.org/10.1029/2001wr000826

Hale, M. G., & Orcutt, D. M. (1987). *The physiology of plants under stress*. John Wiley & Sons.

He, Q., Li, S., Kang, S., Yang, H., & Qin, S. (2018). Simulation of water balance in a maize field under film-mulching drip irrigation. *Agricultural Water Management*, *210*, 252–260. https://doi.org/10.1016/j.agwat.2018.08.005

Hupet, F., Lambot, S., Javaux, M., & Vanclooster, M. (2002). On the identification of macroscopic root water uptake parameters from soil water content observations. *Water Resources Research*, *38*(12), 36–36-14. https://doi.org/10.1029/2002wr001556

Karandish, F., & Šimůnek, J. (2016). A field-modeling study for assessing temporal variations of soil-water-crop interactions under water-saving irrigation strategies. *Agricultural Water Management*, *178*, 291–303. https://doi.org/10.1016/j.agwat.2016.10.009

Lamm, F. R., Bordovsky, J., Schwankl, L., Grabow, G., Enciso-Medina, J., Peters, R., et al. (2012). Subsurface drip irrigation: Status of the technology in 2010. *Transactions of the ASABE*, *55*(2), 483–491. https://doi.org/10.13031/2013.41387

Latif, M., Haider, S. S., & Rashid, M. U. (2016). Adoption of high efficiency irrigation systems to overcome scarcity of irrigation water in Pakistan: Adoption of high efficiency irrigation systems. *Proceedings of the Pakistan Academy of Sciences: Part B (Life and Environmental Sciences)*, *53*(4), 243–252.

Lehmann, E. L., & Casella, G. (1998). *Theory of point estimation* (2nd ed.). Springer.

Li, W., Wainwright, H. M., Yan, Q., Zhou, H., Dafflon, B., Wu, Y., et al. (2021). Estimation of evapotranspiration rates and root water uptake profiles from soil moisture sensor array data. *Water Resources Research*, *57*(11), e2021WR030747. https://doi.org/10.1029/2021WR030747

Lu, Z., Neuman, S. P., Guadagnini, A., & Tartakovsky, D. M. (2002). Conditional moment analysis of steady state unsaturated flow in bounded, randomly heterogeneous soils. *Water Resources Research*, *38*(4), 9-1–9-15. https://doi.org/10.1029/2001WR000278

Martín, J., Sáez, J. A., & Corchado, E. (2021). On the suitability of stacking-based ensembles in smart agriculture for evapotranspiration prediction. *Applied Soft Computing*, *108*, 107509. https://doi.org/10.1016/j.asoc.2021.107509

Pan, M., & Wood, E. F. (2006). Data assimilation for estimating the terrestrial water budget using a constrained ensemble Kalman filter. *Journal of Hydrometeorology*, *7*(3), 534–547. https://doi.org/10.1175/jhm495.1

Parajuli, K., Jones, S. B., Tarboton, D. G., Flerchinger, G. N., Hipps, L. E., Allen, L. N., & Seyfried, M. S. (2019). Estimating actual evapotranspiration from stony-soils in montane ecosystems. *Agricultural and Forest Meteorology*, *265*, 183–194. https://doi.org/10.1016/j.agrformet.2018.11.019

Perrochet, P. (1987). Water uptake by plant roots—A simulation model, I. Conceptual model. *Journal of Hydrology*, *95*(1–2), 55–61. https://doi.org/10.1016/0022-1694(87)90115-6

Porporato, A., D'Odorico, P., Laio, F., & Rodriguez-Iturbe, I. (2003). Hydrologic controls on soil carbon and nitrogen cycles. I. Modeling scheme. *Advances in Water Resources*, *26*(1), 45–58. https://doi.org/10.1016/S0309-1708(02)00094-5

Reichle, R. H., Crow, W. T., & Keppenne, C. L. (2008). An adaptive ensemble Kalman filter for soil moisture data assimilation. *Water Resources Research*, *44*(3). https://doi.org/10.1029/2007wr006357

Sampathkumar, T., Pandian, B., & Mahimairaja, S. (2012). Soil moisture distribution and root characters as influenced by deficit irrigation through drip system in cotton–maize cropping sequence. *Agricultural Water Management*, *103*, 43–53. https://doi.org/10.1016/j.agwat.2011.10.016

Sinsbeck, M., & Tartakovsky, D. M. (2015). Impact of data assimilation on cost-accuracy tradeoff in multifidelity models. *SIAM/ASA Journal on Uncertainty Quantification*, *3*(1), 954–968. https://doi.org/10.1137/141001743

Tartakovsky, D. M., Guadagnini, A., & Riva, M. (2003). Stochastic averaging of nonlinear flows in heterogeneous porous media. *Journal of Fluid Mechanics*, *492*, 47–62. https://doi.org/10.1017/S002211200300538X

Tartakovsky, D. M., Lu, Z., Guadagnini, A., & Tartakovsky, A. M. (2003). Unsaturated flow in heterogeneous soils with spatially distributed uncertain hydraulic parameters. *Journal of Hydrology*, *275*(3–4), 182–193. https://doi.org/10.1016/s0022-1694(03)00042-8

van Genuchten, M. T. (1980). A closed-form equation for predicting the hydraulic conductivity of unsaturated soils. *Soil Science Society of America Journal*, *44*(5), 892–898. https://doi.org/10.2136/sssaj1980.03615995004400050002x

Vrugt, J. A., Hopmans, J. W., & Šimunek, J. (2001). Calibration of a two-dimensional root water uptake model. *Soil Science Society of America Journal*, *65*(4), 1027–1037. https://doi.org/10.2136/sssaj2001.6541027x

Vrugt, J. A., van Wijk, M. T., Hopmans, J. W., & Šimunek, J. (2001). One-two-and three-dimensional root water uptake functions for transient modeling. *Water Resources Research*, *37*(10), 2457–2470. https://doi.org/10.1029/2000wr000027

Wang, P., & Tartakovsky, D. M. (2011). Reduced complexity models for probabilistic forecasting of infiltration rates. *Advances in Water Resources*, *34*(3), 375–382. https://doi.org/10.1016/j.advwatres.2010.12.007

Wilson, K. B., Hanson, P. J., Mulholland, P. J., Baldocchi, D. D., & Wullschleger, S. D. (2001). A comparison of methods for determining forest evapotranspiration and its components: Sap-flow, soil water budget, eddy covariance and catchment water balance. *Agricultural and Forest Meteorology*, *106*(2), 153–168. https://doi.org/10.1016/s0168-1923(00)00199-4